Electron-induced ionization and cationic fragmentations of the isolated molecule of 2,4-imidazolidinedione (Hydantoin) : Study of the relaxing paths thresholds.

Jean-Philippe Champeaux, Patrick Moretto-Capelle, Julie Renoud, Laurent Polizzi, Stéphane Faure, Daniel Castex, Michel Gianesin, Eric Panader, Philippe Paquier, William Volondat, et al.

Electron-Induced ionization and cationic fragmentations of the isolated molecule of 2,4-imidazolidinedione (Hydantoin) : Study of the relaxing paths thresholds.

J.-P. Champeaux *[a], P. Moretto-Capelle [a], J. Renoud[a], L. Polizzi[a], S. Faure[a], D. Castex[a], M. Gianesin[a], E. Panader[a], P. Paquier[a], W. Volondat[a], T. Salbaing[b], J. Riffaud[c], R. Point[a], P. Cafarelli[a], M. Sence[a].

[a] Laboratoire Collisions Agregats et reactivité, UMR 5589-CNRS Université Paul Sabatier Toulouse III, 118 Route de Narbonne, 31062 TOULOUSE Cedex 9, France
[b] Hospices Civils de Lyon ,Service de Radiothérapie-Oncologie,165 chemin du grand revoyet 69495 PIERRE BENITE cedex, France
[c] CEA, DAM, DIF, F-91297 ARPAJON

In this work, our new experimental setup has been used to study the ionization and fragmentation of the prebiotic molecule hydantoin by electron impact. Scanning of the incident electron energy allows the determination of the appearance thresholds of the cations. The vertical ionization potential was found to be in good agreement with previous data. Dissociation thresholds for the main fragmentation patterns were also measured. In parallel, thanks to quantum chemical calculations, reaction schemes compatible with the experimental results are given.

1. Introduction

Many complex molecules composed of carbon and hydrogen could be abundant in the interstellar medium, such as polycyclic aromatic hydrocarbons (PAHs), whose infrared signatures seem compatible with the infrared spectra emitted by some nebulae[1–4]. In the circumstellar environment, many organic molecules have been identified[5,6].

The physical chemistry of these organic molecules is not yet fully understood and is the starting point for many studies on their formation processes[7,8] as well as their life cycle and destruction in astrophysical media[9–11].

In the vicinity of the Sun, some molecules of biological interest have recently been detected, such as the amino acid glycine, ejected by the comet 67P/Churyumov-Gerasimenko (Chury) and detected by the Rosetta mission[12]. Such molecules, called prebiotic molecules, may have played a role in origin of life. Among them,

2,4-imidazolidinedione molecule named Hydantoin ($C_3N_2O_2H_4$, m=100 a.m.u) was identified with traces of glycine in samples of two meteorites, Murchinson and Yamato[13,14], showing its presence in circumstellar environment (not detected in Chury comet).

Laboratory studies by De Marcellus et al[15] clearly show that hydantoin molecules can be produced by UV irradiating water ice containing methanol (CH_3OH) and ammonia (NH_3). Ice grains simulate interstellar grains present in the cometary formation region. Kayanuma et al[16] also propose in their theoretical study that hydantoin can be formed from aminoacetonitrile ($C_2N_2H_4$) under cold astrophysical conditions, when the comets are heated by a neighboring star. Thus, if hydantoin can be assumed to be formed in space by various mechanisms, we need to consider the effect of stellar ionizing radiation and the corresponding molecular modification it can induce.

The electronic structure of hydantoin (and derivatives) was investigated by Vondrack et al[17] by photoelectron spectroscopy after HeI irradiation. The ionization potential as well as the energies of the first excited states were derived.

Ildiz et al.[18] isolate the molecule in Ar matrix at low temperature (10K), they realize infrared spectroscopy, which has been understood by accompanying theoretical investigation, but also by irradiation with 230 nm (5.4 eV) radiation: IR analysis after irradiation reveals three bodies fragmentation into isocyanic acid (HNCO), carbon monoxide (CO) and methylenimine ($HNCH_2$).

While X-UV irradiation of prebiotic and organic molecules has been intensively studied in an astrophysical context[19], the effect of charged particles (electrons, ions) that make up the stellar winds has received less interest. The ionization and fragmentation of the hydantoin molecule induced by interactions with minority species of the solar wind, namely the multicharged ions O^{6+} and He^{2+}, through a multi-ionization/excitation process has been investigated in a previous paper[20].

In this work, we study both experimentally and computationally the interaction of isolated neutral hydantoin with one of the most abundant species in the solar wind: electrons whose energies range from 8eV to 40eV. We will focus on the (e-,2e-) processes corresponding to the reaction scheme (1) above, considering only single ionization events of the molecule:

$$e_i^- + \mathrm{C_3N_2O_2H_4} \rightarrow e_i^{-*} + \mathrm{C_3N_2O_2H_4^{+*}} + e^-$$
$$\mathrm{C_3N_2O_2H_4^{+*}} \rightarrow A^+ + \{B°\} \quad (1)$$

Here, e_i^- is the incoming electron from the stellar wind, e_i^{-*} the diffused electron after the interaction with hydantoin, $C_3N_2O_2H_4^{+*}$ the ionized and excited molecule, e^- the emitted electron from the molecule to the continuum, A^+ and {B°} respectively the cationic and neutral(s) fragment(s) produced after molecular relaxation by dissociation. Single ionization as well as cationic fragmentation thresholds have been measured and will be presented in this paper. For each of the observed A^+ formed cations, a possible corresponding reaction scheme will be refined by theoretical investigations.

2. Experimental setup and data analysis

The SWEET experimental setup is a crossed-beam experiment dedicated to the study of the interactions between an isolated molecule and an energetic electron (or ion - but not used in this work -) whose energy can be adjusted to "simulate" the energy distribution of stellar winds. The entire experiment is maintained under vacuum, typically 10^{-7} Torr.
The Earth's magnetic field inside the chamber is compensated using a Mu Metal shielding and external Helmholtz coils. Less than 4 mG of residual magnetic field is present in any direction inside the interaction chamber. Figure 1 shows a schematic view of the SWEET collision chamber.

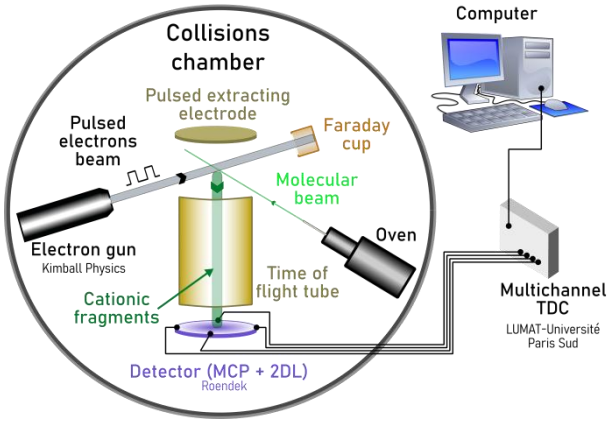

Fig. 1 - Schematic view of the SWEET experimental part used in this study

The electron beam is generated by a commercially available Kimball Physics electron gun. The electronic current can be measured by means of a Faraday cup which is placed in front of the electron gun, after the collision zone. The energy range of the gun is 2 eV to 2 keV, with an energy spread of 0.5 eV (given by the manufacturer). The electron beam is pulsed (KHz) for synchronization purposes; this is ensured by a constant negative potential applied to the grid electrode (Wehnelt) of the gun, on which we superimpose a positive nanosecond pulse coming from a homemade circuit detailed in Fig. 2, based on a ZTX415 avalanche transistor.

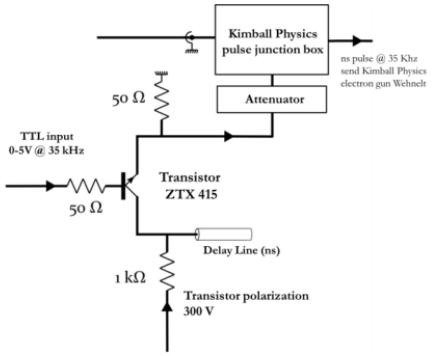

Fig. 2 - Electronic scheme of the fast (ns) pulse generator ***[Zetex,application note 1996]***

The amplitude of this signal is set so that the grid potential is positive and allows the electrons to exit during the tuneable (via delay line choice) time duration of the pulse. The temporal width of the generated electron pulse was measured directly by the time-of-flight at a fixed electron energy using the SWEET high-resolution dispersive electron spectrometer (not shown in Fig. 1). An example of a 2.8 ns electron pulse at 35 kHz for 100 eV electrons obtained with this circuit is shown in Fig. 3.

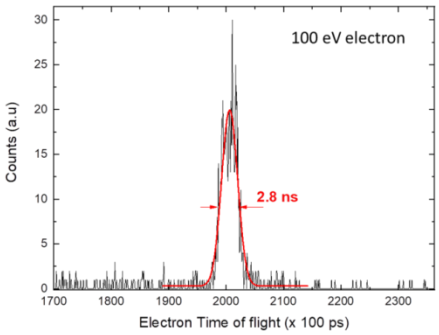

Fig. 3 - Example of measured electron beam pulse width for 100eV electrons

Commercial hydantoin powder (Sigma-Aldrich, 98% purity) is sublimated in an oven to produce the effusive jet of the neutral molecule. The geometry of the molecular jet produced by the oven was studied as a function of temperature for the same vacuum conditions as in SWEET (10^{-7} Torr) and the same distance from the oven capillary to the interaction zone, using a specific setup. The optimal conditions to obtain a thin hydantoin molecular jet (less than 2 mm width in the interacting region) were found at 423 K (PT100 sensor) and used in the SWEET setup. At this temperature, assuming thermodynamic equilibrium inside the oven, the total internal thermal energy of the hydantoin molecule is 0.98 eV, evenly distributed in the different degrees of freedom of the molecule. This is not enough (statistically speaking) to change its geometry has been discussed in previous paper[20] where the activation barrier of the first conformers are calculated. It is then reasonable to assume that the hydantoin molecule will be produced in its electronic ground state (neutral) and in the absence of any conformation. The molecule in its fundamental geometry is shown in Figure 4.

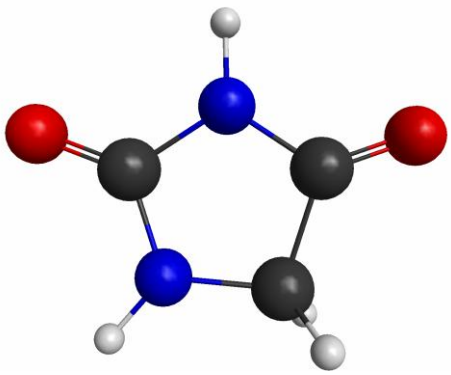

Fig. 4 - Initial geometry of neutral Hydantoin.

After each electron/molecule interaction, the cations emitted from the molecule are mass over charge analysed using a home-built 250mm time-of-flight mass spectrometer (TOF-MS) based on a modified Wiley MacLaren TOF with second order time focusing (see Figure 1). The extracting and spatial focusing electrodes are pulsed with an appropriate delay to the electron pulses coming from the electron gun to ensure that the electrons are out of the collision zone when the cationic fragments are extracted. This avoids perturbation of the electrons prior to interaction and ensures that all ions generated during the passage of a given electron packet are extracted simultaneously: there is no TOF difference between an ion of a given m/q formed at the beginning of the electronic pulse and the same ion formed at the end of the pulse, so that the temporal resolution is not much reduced by the temporal width of the electronic pulse.

The TOF detector consists of two 40 mm diameter microchannel plates (MCP from Hamamatsu Ltd.), resulting in a gain of ~10^7 electrons per detected ion. The MCPs are followed by two perpendicular delay lines (Roendeck Ltd.). These form a two-dimensional position sensor in the two orthogonal directions (denoted X and Y) perpendicular to the TOF drift-tube axis (denoted Z). The impact position X (or Y) of an ion is directly related to its initial velocity perpendicular to the TOF axis: vx (or vy) and the vz component along z can also be derived from the applied extraction field E alond z direction:

$$\begin{cases} V_x = \dfrac{X}{TOF} \\ V_y = \dfrac{\mathrm{Y}}{\mathrm{TOF}} \\ V_z = -\dfrac{qE}{m}(T - T_0) \end{cases}$$

where T_0 is the flight time of the particle of mass m without velocity.

The signals coming out of the delay line pass through an electronic pre-amplifier (home-made) and a discrimination system before being analyzed by a 120 ps resolution time-digital converter (TDC) developed by the LUMAT Federation at the Université Paris Sud, France. For each packet of electrons, an acquisition is triggered by the frequency command. The acquisition time (typically 7.6 µs) is defined by the flight time of the heaviest ion.
In order to obtain the efficiency curves of the cations presented in this work, the electron energies E are scanned from 8 eV to 20 eV with a step of 0.5 eV. A mass spectrum is recorded at each energy step and the intensity of each peak corresponding to a particular cationic molecule fragment is plotted against electron energy. To calibrate the energy scale, the presence of residual water with a known vertical ionization potential (12.62 eV[21]) was used. Energy calibration was also performed by injecting helium, which has a known ionization potential (24.58 eV). The appearance energy thresholds (AE) of cationic species are obtained by fitting the near-threshold efficiency curves with a Wannier threshold law surimposed on a linear background[22,23]:

$$\begin{cases} f(E) = kE + b & (E < AE) \\ f(E) = kE + b + c(E - AE)^p & (E \geq AE) \end{cases}$$

where E is the electron energy, k and b are the linear background coefficients, c is the slope of the threshold, and p is the Wannier exponent, which has been theoretically found to be 1.127 for the hydrogen atom[22] .

3. Computational details

In order to help us determine which fragmentation is the most likely to occur, quantum chemical calculations were carried out using the GAMESS code[24]. Density Functional Theory using the B3LYP functional, together with the 6-311G++(d,p) basis set, was used for all calculations and is known to be accurate for such small, organic molecules[25,26]; in Russo et al[26] an estimate of the error can be obtained by comparing the experimental and calculated proton affinities in aniline and is about 0.15eV. In a previous paper on solar wind minority ion/hydantoin collisions, some of the calculations presented in this paper were already introduced[20].
The relaxed geometries of each detected ion of mass m and the complementary neutral fragment(s) of mass 100-m were calculated as well as the corresponding electronic energies. In contrast to previous work, the zero-point vibrational energy (ZPVE) is not included here. This is because we focus on the electronic excitation of the molecule. This could cause small shifts in the calculated energy levels corresponding to relaxed geometries, typically a few tens of eV.
We are aware that the initial physical process is ionization and molecular electronic excitation, i.e. population of electronic excited states (hole in molecular orbitals). These excited states evolve and, after complex molecular mechanism(s), fragmentation takes place. Pitzer et al.[27], in the one-photon protonated uracil interaction in the 4.5-9.5eV range, show that the yield of a given mass shows maxima that can be correlated to excited states.
Note that we only evaluate vertical excited states. The complete energy transfer mechanisms are beyond the scope of this publication. However, it is known that internal conversion mechanisms such as conical crossings are responsible for ultrafast conversion of excited states to ground state vibrational modes. Numerous studies [28] on neutral molecule shave been devoted to nucleic acid (the structure of hydantoin is very close to the pydimidic bases) due to their remarkable photostability.
For the uracil cation, Matsika[29] found a two- and three-state conical intersection in uracil$^+$ between the ground state and the D1 excited state, and between the ground D0 state and the D1 and D2 excited states.
Segarra-Marty et al[30] improved on the previous results and extended the studies to the thymine cation a few years later. In their paper, the authors present the evolution of the D0, D1, D2 states potential energy surfaces and predict the evolution of the initial D2 population to the ground D0.
These studies show that, through the conical intersections, the electronic excitation energy is found in the vibrational states of the molecule at the ground level. Few data exist on hydantoin molecule, however Su[31] has demonstrated a conical intersection between the ground state and the first excited state of the neutral molecule, allowing to explain the fragmentation observed by Ildiz et al[18].
In this work we propose reaction pathways from the initial ionized hydantoin electronic ground state (after Internal Conversion process from excited states) to the experimentally observed cationic fragmentations.
For this, the possible transition states along each pathway were determined and Internal Reaction Coordinate (IRC) calculations were performed to ensure the connection between the intermediate minima of the potential surface (i.e., corresponding to intermediate molecular conformations) before and after each pathway transition point. If the activation barrier for a transition state from the initial or final intermediate conformation is too high, typically >1eV, a DRC calculation, taking into account the kinetic energy release during the process, is performed to ensure that the molecular geometries between the transition points can be reached without major changes in the molecular structure such as fragmentation and rearrangement.
For each proposed reaction pathway, we tried to minimize the number of intermediate transition states (and the height of their activation barriers) required to dissociate the molecule into two fragments: a cation corresponding to the measured one and its

complementary neutral fragment. The final charges of the resulting fragments are deduced from the sum of Mulliken atomic charges.
The highest energy point of each calculated reaction trajectory (transition state or dissociation energy) must be less or equal to the measured appearance energy thresholds for each cation.

4. Experimental results and discussion

4.1 Mass Spectrum

Mass Spectrum The mass spectrum obtained after interaction of a neutral hydantoin molecule with a 100eV electron beam is shown in Fig. 5.

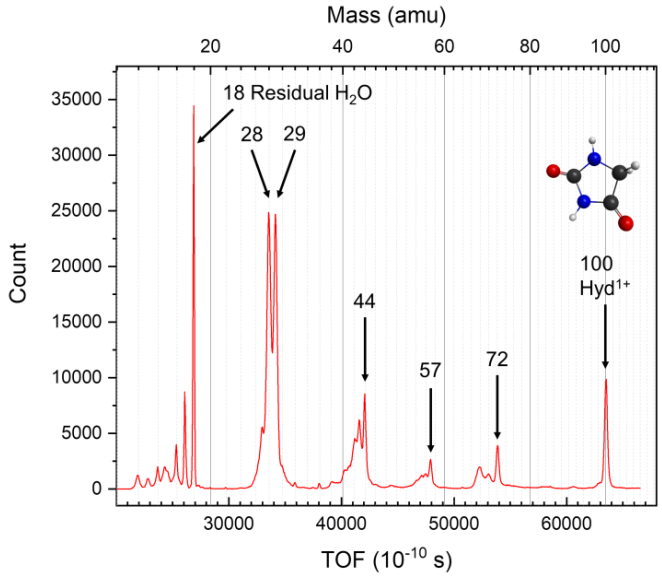

Fig. 5 - 100eV electron impact ionisation mass spectrum obtains from neutral Hydantoin molecule. The parent ion Hyd^{1+} (at 100 amu) as well as the principal mono-cationic fragments and the residual water are labelled by their mass in atomic mass unit.

The incident electron energy (100 eV) is much higher than the first ionization potential (IP) of the molecule (10 eV see section 4.4). The mass spectrum shown in Figure 5 is therefore an integrated mass spectrum over this range of possible initial excitation energies.
The origin of the cation is essentially derived from the process of ionization and its fragmentation. As shown by Tian[32], who gives a $\sigma_{ion\ pair}/\sigma_{photoionization} \approx 10^{-2}, 10^{-5}$, the formation of positive-negative ion pairs is completely negligible. In our study on the fragmentation of halo-uracil by proton impact at 100 keV (same velocity than 54eV electrons), we explicitly searched for the presence of anions, which turns out to be negative despite the presence of halogen in the molecules[33].
The five major cationic fragments discussed in this paper are labelled with their atomic masses in Fig. 5: 28, 29, 44, 57 and 72 a.m.u. The non-fragmented parent cation Hydantoin$^+$ (m/z 100 amu) is also observed. For these cations, the appearance threshold has been measured and the corresponding reaction pathway leading to these ions has been calculated.
The peak corresponding to residual water (H_2O^+, 18 amu) is also observed, but is not due to hydantoin dissociation. It will be used for the calibration of the energy scale for the determination of the thresholds of the hydantoin fragments.
The relative abundances of the fragments (Branching Ratios) are in agreement with the NIST data recorded at 75 eV. Except for the 44 amu fragment, which is slightly higher than the 43 amu fragment. However, resolution effects may account for this difference.
The mass spectrum in Fig. 5 is also comparable to those obtained after the interaction of hydantoin with minority ions of the solar wind He^{2+} at 8 keV and O^{6+} at 30 keV[20] , but in the latter case a stronger population of Hyd^+ is observed as well as a smaller population of small fragments such as 28^+ and 29^+. These differences can be explained by the lower amount of energy deposited in the molecule in the case of multi-charged ion collisions. This is due to the larger impact parameters involved.

4.2 Comparison with pyrimidic bases

The hydantoin molecule is very similar to the uracil molecule: one atom of the hexagonal ring is removed and the hydrogen atom attached to it is transferred to the neighboring carbon.

The fragmentation of cationic pyrimidine bases produced by electron impact has been intensively studied: HNCO emission is clearly observed with uracil but no CO emission[23]. The same main channel is also found in thymine[34]. Theoretically, Zhou et al.[35] investigate ground-state fragmentation pathways of uracil cation, showing initial HNCO emission from uracil cation and the possibility of further fragmentation processes. In cytosine, strong emission of neutral CO at 70eV collision energy is observed as well as HNCO[36] which requires hydrogen transfer from -NH2; their paper presents calculations of isomerization (ring opening) scheme and dissociation path (with corresponding transition state).

In collisions with 100 keV protons A Le Padellec et al[37], HNCO° emission is observed in uracil and thymine, 28^0 emission in cytosine, and the 28^+ fragment predominates in all pyrimidine bases. In multiphoton ionization of uracil, Ryszka et al.[38] investigate this fragmentation channel and, thanks to high-resolution mass spectrometry, show that the chemical nature of the cation 28^+ is $HNCH^+/NCH_2^+$ rather than CO^+.

4.3 Kinetic energies spectra of fragments

The kinetic energies of the fragments can be measured using the 3D Velocity Mapping Imaging technique.

The event by event mode allows us to measure the position of the impact on the detector as well as the time of flight of each cation detected.

The 3D velocity vector and the mass of the cation are derived from these measurements. In Fig. 6 we present the 2D (X,Y) velocity distributions (resulting from the impact of the position on the detector) for the unfragmented hydantoin cation 100^+ and for the 28^+ cation for 100eV impact energy. The kinetic energy distribution is obtained from the statistical analysis of the kinetic energy (issued from 3D velocity) determined for each event

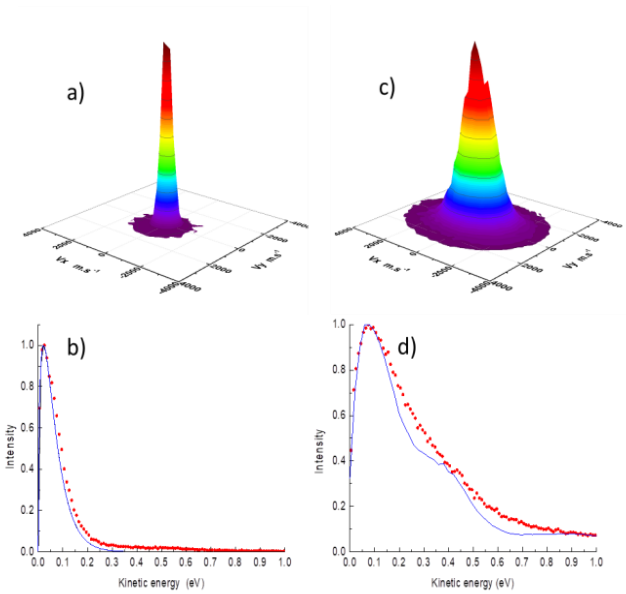

Fig. 6- Velocity distribution in the X-Y plane for Hyd^+ (a) and 28^+ (c). Experimental kinetic energy distribution (red), Boltzmann distribution for Hyd^+ (b) and deconvolution for 28^+ (blue) (d)

For the unfragmented cation, the experimental distribution is compared with the Boltzmann distribution at T=150°C (which corresponds to the oven temperature) and good agreement is found.

For the 28^+, the experimental distribution $D(E_{lab})$ is broader. This indicates a higher kinetic energy for this fragment. The experimental distribution also reflects the temperature broadening of the initial unfragmented molecule. In order to avoid this, we use a deconvolution of the energy distribution. For a given energy E and a corresponding velocity V of the fragment in the original cation frame, the energy in the laboratory frame is given by:

$$E_{lab} = \frac{1}{2}.m * \left|V * \vec{e}_{rand} + \vec{V}_{ic}\right|^2$$

Where e_{rand} is a unitary vector randomly oriented in space and V_{ic} is the thermal velocity of the initial 100^+ cation. The corresponding distribution $R(E_{lab},E)$ can be calculated and follows the distribution of V_{ic} measured. Therefore, we can write:

$$D(E_{lab}) = \sum R(E_{lab}, E_i).D(E_i)$$

where $D(E_i)$ represents the distribution without thermal broadening. The Scofield algorithm, as presented by Sampoll[39] is used to invert these relations to obtain D(Ei). The result is shown in Fig.6. There is an important peak at 80meV and a less intense one at 0.35eV, this could be an indication of a dissociation scheme where, for example, a transition state is involved and the available kinetic energy (KER) is distributed among the fragments.

4.4 Cationic fragments appearance energies

Fig. 7 shows the mass spectra measured at different electron energies and the measured efficiency curves (black dots) for the hydantoin cation and the five major fragments (72, 57, 44, 29 and 28 amu). The fitted curve obtained by the method described in section 2 is plotted as a red solid line and the resulting E_{AP} is indicated by arrows. The error given by the numerical fit gives the uncertainty of each E_{AP} value. The measured Hyd^+ appearance energy corresponds to the first vertical ionization energy, i.e. the energy required to remove an electron without rearranging the geometry of the nucleus. The appearance energies are summarized in Table 1.

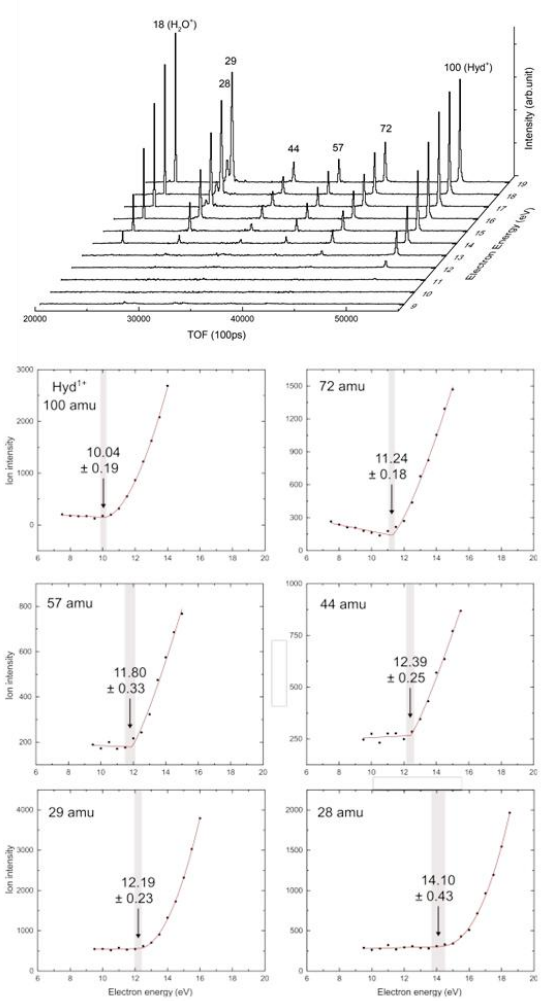

Fig. 7 - Mass spectra as a function of the incident electron energy and corresponding measurements of appearance thresholds for observed 100,72,57,44,29 and 28 a.m.u cations

It should be noted that only low energy thresholds have been studied and that other channels of fragmentation may exist at higher energies.

Table 1 – Measured appearance energies (AE) extracted from Fig.7

Mass (amu)	AE (eV)
100 (Hyd^+)	10.04 ± 0.19
72	11.24 ± 0.18
57	11.80 ± 0.33
44	12.39 ± 0.25
29	12.19 ± 0.23
28	14.10 ± 0.45

4.5 Breakdown curves

Breakdown curves vs. electron energy derived from Figure 7 are shown in Figure 8 for the studied fragmentation channels. The curves associated with 72^+ (emission of neutral CO), 57^+ (emission of neutral HNCO) show a broad maximum, indicating that further fragmentation occurs, while the curve associated with 100^+ cation decreases continuously with electron energy, as expected. The curve associated with 44^+ starts to rise from its threshold and then remains almost constant above 14eV. On the other hand, the curves associated to 29^+ and 28^+ cations show a continuous increase.

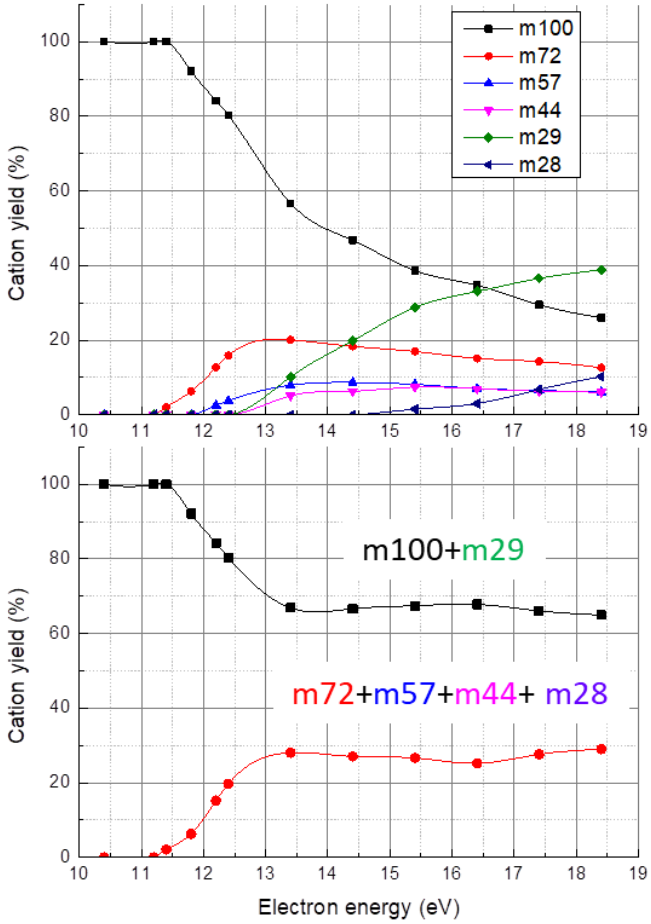

Fig. 8- Breakdown curves for the dissociation of Hyd^+ vs incident electron energy

In search of possible fragmentation schemes looking for parent and daughter ions, we have summed different channels: it seems that the sum of unfragmented cation 100^+ and 29^+ is constant above ≈13eV, suggesting a direct formation of 29^+ directly from 100^+ parent. The decrease of 72^+ coincides with the increase of 44^+, the same is true for 57^+ and 28^+ at the threshold, but the strong increase of 28^+ at higher energies is essentially related to the decrease of the population of 72^+ (73%) and 57^+ cation (27%).

5. Theoretical results and discussions on the possible reaction scheme

5.1 Initial molecular excited states

The first seven excited states of the hydantoin cation molecule have been evaluated by means of TDDFT calculation. Vertical transitions from the ground state of the neutral molecule to these excited states are summarised in Table 2 with corresponding orbital bases decompositions, excited states are clearly associated with vacancy formation in the inner molecular orbitals.

Table 2 – Calculated energies of excited states with TDDFT and corresponding main orbital contribution

States	Vertical Excitation energy (eV)	Composition
D0	10.00	100% (Homo)
D1	10.15	92% (Homo -1)
D2	10.67	92% (Homo -3) + 7% (Homo -2)
D3	11.06	70% (Homo -2) + 22% (Homo -3)
D4	13.61	92% (Homo -4)
D5	14.25	92% (Homo -5)
D6	14.41	91% (Homo -6)
D7	14.84	90% (Homo -7)

With a global shift of only 0.2eV, the calculated excitation energies agree with the photoelectron spectrum of hydantoin provided by Vondrak et al[17].
Comparing Table 1 with Table 2, it can be seen that the appearance energies (AE) of the cationic fragments with masses 72 and 57 are compatible with the third excited state of Hyd^+, whereas 44, 29 require a higher initial electronic excitation: the nearly excited state D4 of Hyd^+. The composition of this cationic exited state, 90% of Homo-4, shows that this state excitation is close or equivalent to a direct initial ionization of the Homo-4 orbital from the neutral hydantoin.
The 28^+ a.m.u. cation has the highest AE with 14.10 eV. This requires an initial excitation greater than D5, corresponding to the initial homo-5 ionization from the neutral molecule.

5.2 Cation m/z 100 : ionization of hydantoin

The first vertical ionization potential of the hydantoin was measured to be $AE_{-100}^+ = 10.04 \pm 0.19$ eV. This experimental result is in agreement with the quantum chemical calculation of the vertical ionization energy, which was performed with the computational methods described in section 3, and which gives $E_{AP\text{-}100}^+ = 10.0$ eV as shown in Fig. 7. Our measurement is also in good agreement with previous studies: the experimental study by Vondrack et al[17] using photoelectron spectroscopy gives an $AE_{-100} = 10.20$ eV, and the theoretical work by Bacchus-Montabonel[40] using CASSCF/6-311G** gives 9.91 eV, as summarized in Table 3.

Table 3 – Comparison of $Hydantoin^+$ AE values obtained experimentally and theoretically in this work with values obtained in previous studies.

Author	Type	Method	AE(eV)
Present work	Exp.	Electron impact	10.04 +/- 0.19
Renoud et al[20].	Th.	DFT(B3LYP) 6-311++G(d,p)	10.00
Bacchus-Montabonel[40]	Th.	CASSCF 6-311G**	9.91
Vondrak et al.[17]	Exp.	Photo electron spectroscopy	10.20+/- 0.05

The relaxed geometry of Hyd^+ in its electronic ground state was found at 9.79 eV relative to the neutral ground state (Figure 9).
The first isomers of Hyd^+ were calculated. Fig. 9 shows their relaxed geometry, labeled G1 to G4, and their corresponding energies. These isomers have a relatively low activation barrier (labeled TSG1 to TSG4 in Fig. 9). They are energetically accessible from Hyd^+ electronic excited states that are higher than D2 for the G1 and G2 geometries and higher than D3 and D4 for the G3 and G4 geometries, respectively.

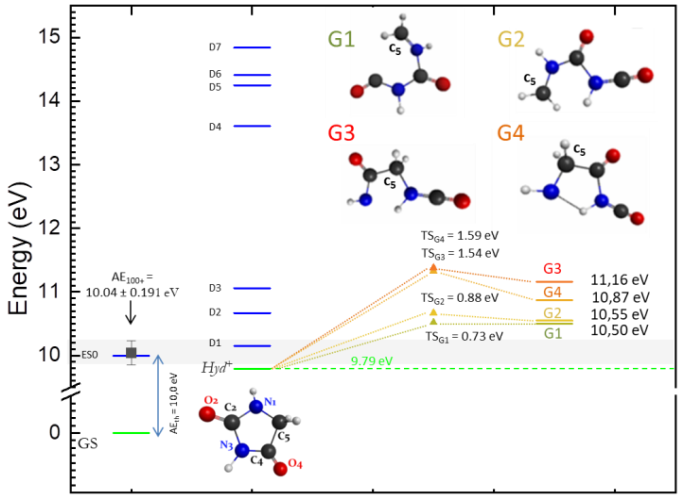

Fig. 9 - Measured and calculated E_{AP} for Hyd^+, transition states energies TS(G1 to G4) relative to Hyd^+ and corresponding relaxed geometries G1 to G4 relative to neutral ground state. The relaxed energy of Hyd^+ (adiabatic ionization potential 9.79eV) is given

5.3 Emission of 72^+

$$e_i^- + C_3N_2O_2H_4 \rightarrow e_i^{-*} + C_3N_2O_2H_4^{+*} + e^-$$

$$C_3N_2O_2H_4^{+*} \rightarrow C_2N_2OH_4{}^+ + CO°$$

The m/z 72 cation is the first molecular fragment to appear at $AE_{72}+$ = 11.24 ± 0.18 eV electron energy, i.e. 1.20 eV above the vertical ionization threshold of neutral hydantoin and close to the third exited state D3 of Hyd^+ calculated at 11.06 eV as shown in Fig. 10.

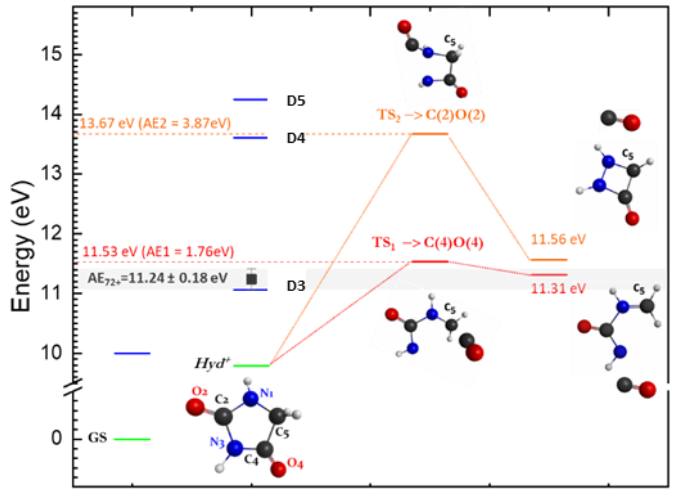

Fig. 10 - Energy diagram with activation energies (E_{AP}) and reaction schemes corresponding transition states (TS1 and 2 respectively) for neural C(2)O(2) and C(4)O(4) emission after Hydantoin single ionization. The excited states of Hyd^+ are noted (Di for i=3 to 5). The experimental Activation energy is EAE_{72+}

In Renoud et al[20] the lowest dissociation limit to produce emission of the neutral mass 28 was attributed to loss of CO rather than HCNH/NCH2. The calculations presented in Fig. 10 are consistent with the emission of the neutral C(4)O(4) fragment: The measured AE_{72}^+ (11.24 ± 0.18) is in good agreement (0.07eV) with the reaction scheme where TS1 is located at 11.61eV and the dissociation limit is calculated at 11.31eV.

5.4 Emission of 57^+

$$e_i^- + C_3N_2O_2H_4 \rightarrow e_i^{-*} + C_3N_2O_2H_4^{+*} + e^-$$

$$C_3N_2O_2H_4^{+*} \rightarrow C_2NOH_3{}^+ + HCNO°$$

As mentioned in Renoud et al[20] there are three simple ways to form HNCO with consecutive atoms in the hydantoin molecule. They are shown in red, orange and green in Fig. 11.

The calculated limits of the dissociation energies corresponding to the fragments $C_2NOH_3^+$ + HNCO in their relaxed geometries and at infinite distances from each other are labeled 1, 2, 3. These dissociation limits are respectively 11.21, 11.95 and 12.82eV from the neutral ground state.

Only dissociations leading to 1 and 2 can energetically match the measured AE of 11.80 ± 0.33eV for the 43°/57^+ fragmentations. The dissociation limit (3) leading to the neutral emission of HN(1)C(2)O(2) is located about 1 eV above the observed AE. No reaction pathway has been found for the formation of this fragment, and attempts to produce it have always resulted in the formation of $OCNH_2^+$.

The measured AE position indicates that the lower dissociation pathway (leading to 1) is not favoured over the pathway leading to HN(3)C(2)O(2), contrary to what was expected in our previous article.

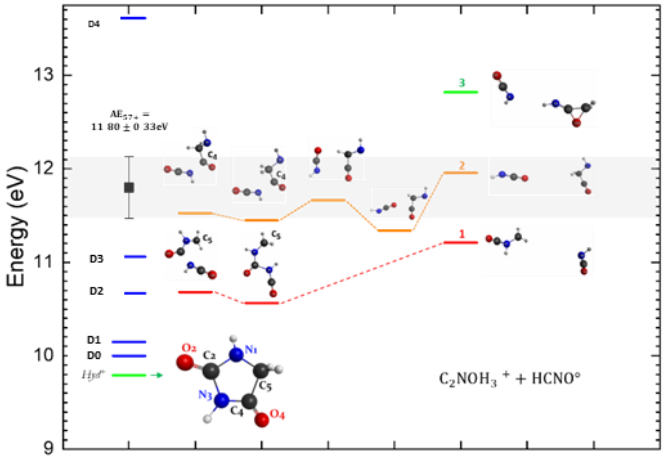

Fig. 11 - Energy diagram and reaction schemes for neutral HCNO emission after Hydantoin single ionization. The excited states of Hyd^+ are noted (Di for i=0 to 5). The experimental activation energy is AE_{43+} .

5.5 Emission of 29^+

Looking for the dissociation leading to $HNCH_2^+$, in a previous work we calculated a dissociation limit where the neutral OC-NH-CO is formed: a 'stable' structure was found[20] with an additional C-C bond formed and the corresponding dissociation limit is 13.6eV. However, this value contradicts our new experimental threshold measured: AE_{29+} =12.19±0.23eV.

We have therefore studied this neutral fragment more closely:

a transition state is found at 0.27 eV relative to the OC-NH-CO ground state, leading to the formation of CO+HNCO, whose energy is 1.53 eV lower than OC-NH-CO one and therefore more stable. The barrier height is quite small (and in the order of the accuracy of the calculations), so we can therefore reasonably assume that the neutral fragment OC-NH-CO does not exist but rather CO and HNCO, the corresponding dissociation energy limit being 12.05eV.

It must be noted that this mode of fragmentation has been experimentally demonstrated by Ildiz et al[18] in the neutral molecule and the conical intersection between the first excited state and the fundamental responsible for this dissociation has been calculated by Su[31].

The measured threshold for this dissociation, AE_{29+} =12.19 0.23eV, is in good agreement with the 'three-body' dissociation limit and is also very close to the thresholds leading to CO (0.9eV higher) and HNCO (0.4eV higher) discussed previously in Sections 5.3 and 5.4, respectively.

In a sequential view of the dissociation process, we could then consider a first initial dissociation with an emission of CO or HNCO. This would be "followed" by a second dissociation of the remaining cations, both leading to $HNCH_2^+$:

$$C_3N_2O_2H_4^{+*} \rightarrow C_2N_2OH_4{}^{*+} + CO° \rightarrow HNCO° + HNCH_2^+ + CO°$$
$$C_3N_2O_2H_4^{+*} \rightarrow C_2NOH_3{}^{*+} + HNCO° \rightarrow CO° + HNCH_2^+ + HNCO°$$

For the initial CO emission, only the lowest energy scheme is retained (n°1 red see Figure 10). This is because the transition state for the higher energy scheme is much higher in energy than the measured threshold.
The same energetic argument applies to the initial neutral HNCO emission, retaining only reaction schemes (1) and (2).

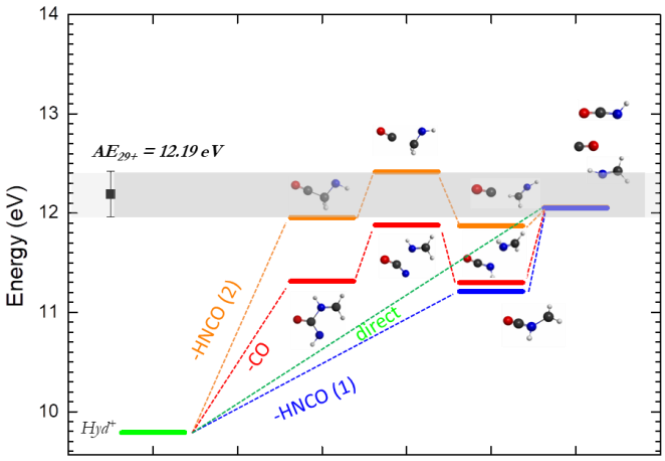

Fig. 12 - Energy diagram and reaction schemes for neutral $HCNH_2$ $^+$ emission after Hydantoin single ionization. The experimental Activation energy is AE_{29+}

Corresponding calculated reaction schemes for the three channels are shown in Figure 12 and are energetically compatible with the measured threshold. Nevertheless, the reaction scheme with initial loss of HNCO after the reaction (1 in Fig. 10) is the simplest one with only one transition state.
However, the breakdown curve (above 13eV) suggests a direct mechanism from hyd$^+$, shown in Figure 12.

5.6 Emission of 44^+

The measured activation energy for 44^+ emission was found to be 12.39 +/- 0.5 eV. In section 5.4, the investigation of the reaction scheme of process 3 leads to the formation of H_2NCO^+ instead of HNCO as shown in Fig. 13. The calculated dissociation limit and activation barrier are two high to match the measured threshold.

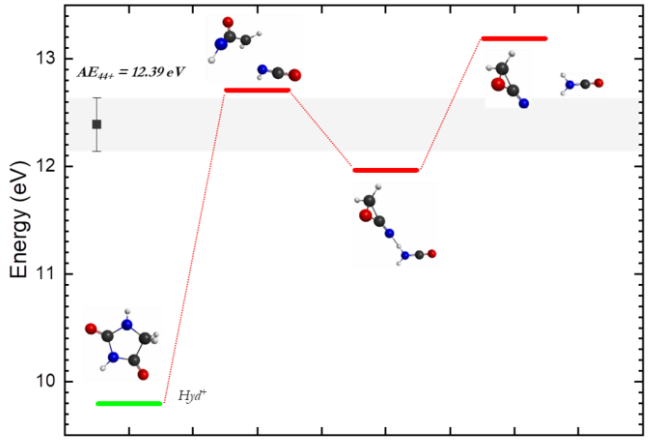

Fig. 13 - Reaction scheme following formation of $OCNH_2^+$ instead of HNCO in pathway (3) of figure 11

Therefore, we investigated the initial conformation of the molecule leading to -OH group as a precursor of HNCOH cation emission: Transition states as well as dissociation limit are much higher than the experimental threshold, such reaction schemes cannot energetically correspond to the emission of 44^+ cation.
The breakdown curve associated with 44^+ formation (see Figure 8) begins to increase as 72^+ begins to decrease, suggesting possible two-step fragmentation:

$$C_3N_2O_2H_4^{+*} \rightarrow C_2N_2OH_4^{+*} + CO$$
$$C_2N_2OH_4^{+*} \rightarrow CNH_2 + OCNH_2^+$$

Three reaction schemes were found and are shown in Fig.14. The red and black ones lead to NCH_2 + $OCNH_2^+$, while the blue one leads to HNCH + $OCNH_2^+$.
These reaction pathways have dissociation limits at 12.08 eV (black and red) and 12.64 eV (blue), which are all energetically compatible with the measured experimental threshold at 12.39 eV. However, we can expect that the black one should be favored, considering that the activation barrier of the red one is slightly higher than the measured threshold as well as the dissociation limit of the blue one.

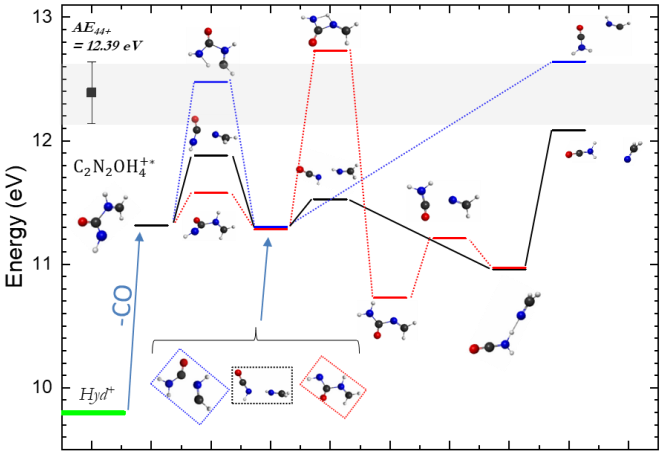

Fig. 14 - Energy diagram and reaction schemes for $OCNH_2^+$ emission after Hydantoin single ionization.

Finally, we can reasonably assume that the emission of 44^+ fragments from hydantoin at the observed threshold corresponds to the emission of the cation $OCNH_2^+$ rather than $HOCNH^+$, given the numerous tentative simulations:

$$C_3N_2O_2H_4^{+*} \rightarrow CO + (NCH_2 or\ HNCH) + OCNH_2^+$$

5.7 Emission of 28^+

The dissociation limit associated with the formation of CO^+ in three-body fragmentation is 16.3eV. This is much higher than the measured experimental appearance threshold for this cation, 14.10eV ± 0.43. This is close to the calculated D5 and D6 excited states of the hydantoin cation. Therefore, the 28^+ fragment must be assigned to the crude formula CNH_2^+,
This is in agreement with the experimental result of Ryszka et al[38] on the multi-photon ionisation of uracil, who show, by means of high-resolution mass spectrometry, that the 28^+ fragment is associated with the $HNCH^+/CNH_2^+$ cation and not with the CO^+ one, due to the small mass difference (28.019 amu and 27.995 amu, respectively).
A possible scenario is to consider, as a first step, the $57^+/49°$ dissociation described in 5.3 (Fig. 10) leading to the $C_2NOH_3^+$ cation (breaking curves analysis indicate that 27% of formation of 28^+ could come from this first step) :

$$C_3N_2O_2H_4^{+*} \rightarrow C_2NOH_3{}^{+*} + HCNO°$$

This is followed by a hydrogen transfer within the $C_2NOH_3^+$ cation before (28+ / 29°) fragmentation to form the $HNCH^+$ cation:

$$C_2NOH_3{}^{+*} \rightarrow HCNH^+ + HCO°$$

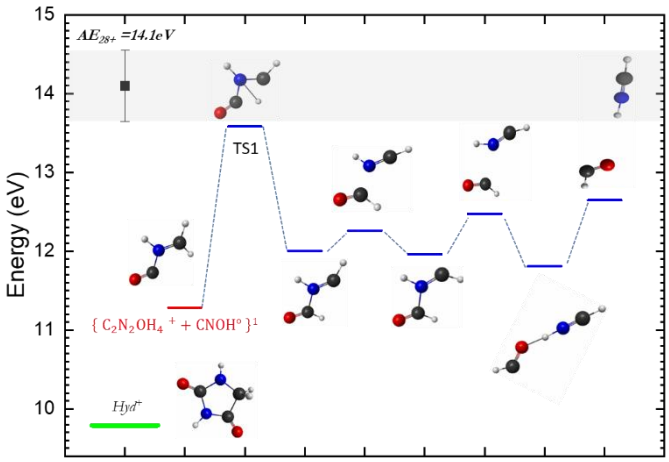

Fig. 15 - hydrogen transfer following emission of neutral HNCO (1 in Fig. 11)

Starting from the two cationic isomers of 57^+ labelled 1 (red) and 2 (orange) in Fig. 11, the corresponding calculated reaction path is shown in Figs. 15 and 16.

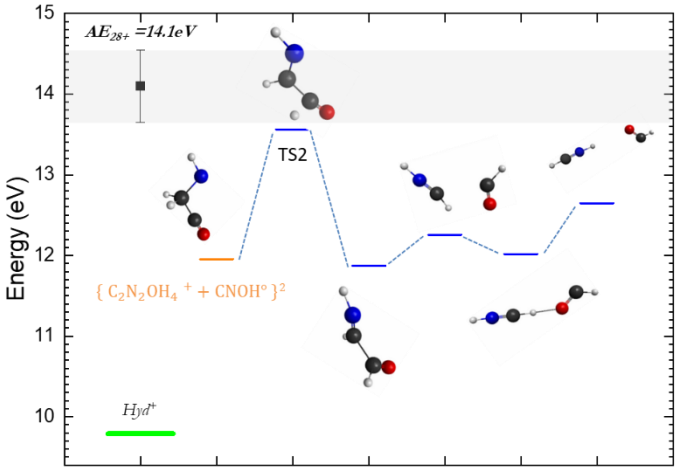

Fig. 16 - hydrogen transfer following emission of neutral HNCO (2 in Fig. 11)

For both reaction schemes, the highest energy point (TS1 and TS2) corresponds to a hydrogen transfer at about 13.6 eV for both cases, which is in reasonable agreement with the measured experimental appearance threshold of 14.1 ± 0.45 eV for the 28^+ cation.

Since the initial transition points are energetically higher than the dissociation limits, the fragments will be able to acquire kinetic energy (this in agreement with the kinetic energy analysis by VMI in paragraph 4.3), so we have performed dynamical reaction coordinate calculations starting from TS1 and TS2 as shown in Figures 15 and 16. The evolution of the trajectories (Figure 17) leads to a spontaneous fast (~200fs) dissociation into $HNCH^+$+HCO. The kinetic energy of fragment 28^+ (center of mass velocity) at the end of the DRC, is 0.09 eV for the scheme shown in Fig. 15 and 0.04 eV for the scheme shown in Fig. 16 due to sharing of the total kinetic energy released between the two fragments and their rotation/ vibration. The value obtained for the first scheme is consistent with the energy of the most intense peak (0.08eV) obtained in paragraph 4.3.

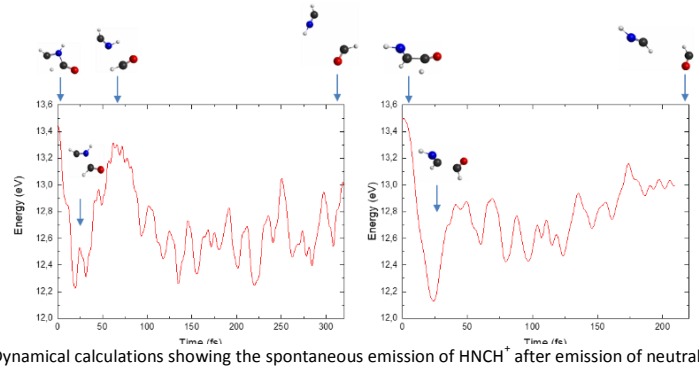

Fig. 17 - Dynamical calculations showing the spontaneous emission of $HNCH^+$ after emission of neutral HNCO°

A second scenario is to consider the emission of CO (73%) as a first step, as suggested by the breaking curve analysis. In Figure 10, the emission of CO could be due to an energetically higher transition state located at 13.67eV, which is consistent with the measured threshold. However, no further fragmentation or hydrogen transfer is observed in the DRC calculation from the TS.

Conclusions

In this work, we have studied the fragmentation of the prebiotic hydantoin molecule induced by the impact of electrons with the help of our new experimental setup SWEET. The dissociation thresholds of hydantoin have been measured for the first time and are used to discriminate between possible reaction schemes suggested by the breakdown curves or calculated for the potential energy surface of the electronic ground state (reached by electronic states after internal transformation).
These new results also refine and/or discriminate fragmentation types from solar wind ion collisions where energetic information was unavailable.

Notes and references

1 A. G. G. M. Tielens, *Annual Review of Astronomy and Astrophysics*,2008,**46,** 289-337
2 M. J. F. Rosenberg, O. Berné and C. Boersma, *Astronomy and Astrophysics*, 2014,**566** ,L4
3 C. Boersma, A. L. Mattioda, C. W. Bauschlicher, E. Peeters, A. G. G. M. Tielens and L. J. Allamandola, *Astrophysical Journal*,2009 , **690,**1208-1221
4 E. Peeters, C. Mackie, A. Candian and A. G. G. M. Tielens, *Accounts of Chemical Research*,2021 , **54(8), *1921-1933***
5 P. Thaddeus, in *Philosophical Transactions of the Royal Society B: Biological Sciences*, 2006, vol. 361.
6 J. Tennyson, *Handbook of Molecular Physics and Quantum Chemistry*, John Wiley Sons, Ldt, Chichester, 2003, vol. 3.
7 C. S. Contreras and F. Salama, *Astrophysical Journal, Supplement Series*,2013 ,**208(1)**
8 E. Reizer, B. Viskolcz and B. Fiser, *Chemosphere*, 2022, **291**, 132793.
9 M. Gatchell, J. Ameixa, M. C. Ji, M. H. Stockett, A. Simonsson, S. Denifl, H. Cederquist, H. T. Schmidt and H. Zettergren, *Nature Communications*,2021 , **12,** 6646
10 J. P. Champeaux, P. Moretto-Capelle, P. Cafarelli, C. Deville, M. Sence and R. Casta, *MNRAS , (2014),***44***,* 1479-1487
11 A. Simon, J. P. Champeaux, M. Rapacioli, P. Moretto Capelle, F. X. Gadéa and M. Sence, *Theoretical Chemistry Accounts*, 2018,**137**,106 ,
12 K. Altwegg, H. Balsiger, A. Bar-Nun, J. J. Berthelier, A. Bieler, P. Bochsler, C. Briois, U. Calmonte, M. R. Combi, H. Cottin, J. De Keyser, F. Dhooghe, B. Fiethe, S. A. Fuselier, S. Gasc, T. I. Gombosi, K. C. Hansen, M. Haessig, A. Jäckel, E. Kopp, A. Korth, L. Le Roy, U. Mall, B. Marty, O. Mousis, T. Owen, H. Rème, M. Rubin, T. Sémon, C. Y. Tzou, J. H. Waite and P. Wurz, *Science Advances*, 2016, **2**
13 G. W. Cooper and J. R. Cronin, *Geochimica et Cosmochimica Acta*, 1995, **59,** 1003-1015
14 A. Shimoyama and R. Ogasawara, *Origins of Life and Evolution of the Biosphere*,2002, **32**, 165-179
15 P. De Marcellus, M. Bertrand, M. Nuevo, F. Westall and L. Le Sergeant D'Hendecourt, *Astrobiology*, 2011, **11,** 847-854
16 M. Kayanuma, K. Kidachi, M. Shoji, Y. Komatsu, A. Sato, Y. Shigeta, Y. Aikawa and M. Umemura, *Chemical Physics Letters*,2017,687,178-183
17 T. Vondrák and C. Cauletti, *Spectrochimica Acta Part A: Molecular Spectroscopy*,1988, **44**, 289-292
18 G. O. Ildiz, C. M. Nunes and R. Fausto, *The Journal of Physical Chemistry A*, 2013, **117**, 726–734.
19 S. Ranjan and D. D. Sasselov, *Astrobiology*,2016 , **16**, 68-88.
20 J. Renoud, S. Indrajith, A. Domaracka, P. Rousseau, P. Moretto-Capelle, B. A. Huber and J. P. Champeaux, *Physical Chemistry Chemical Physics*, 2020, **22**, 5785-5796
21 J. E. Reutt, L. S. Wang, Y. T. Lee and D. A. Shirley, *The Journal of Chemical Physics*, 1986, **85**, 6928-6939
22 G. H. Wannier, *Physical Review*, 1953, **90,** 817-824.
23 S. Denifl, B. Sonnweber, G. Hanel, P. Scheier and T. D. Märk, *International Journal of Mass Spectrometry*, 2004, **238**, 47–53.

24 M. W. Schmidt, K. K. Baldridge, J. A. Boatz, S. T. Elbert, M. S. Gordon, J. H. Jensen, S. Koseki, N. Matsunaga, K. A. Nguyen, S. Su, T. L. Windus, M. Dupuis and J. A. Montgomery, *Journal of Computational Chemistry*, 1993, 1**4**, 1347-1363
25 S. MacLot, D. G. Piekarski, A. Domaracka, A. Méry, V. Vizcaino, L. Adoui, F. Martín, M. Alcamí, B. A. Huber, P. Rousseau and S. Díaz-Tendero, *Journal of Physical Chemistry Letters*, 2013, **4**, 3903-3909
26 N. Russo, M. Toscano and A. Grand, *Journal of Computational Chemistry*, 2000, **21**, 1243-1250
27 M. Pitzer, C. Ozga, C. Küstner-Wetekam, P. Reiß, A. Knie, A. Ehresmann, T. Jahnke, A. Giuliani and L. Nahon, *The Journal of Physical Chemistry A*, 2019, **123**, 3551–3557.
28 C. E. Crespo-Hernández, B. Cohen, P. M. Hare and B. Kohler, *Chemical Reviews*, 2004, **104**, 1977–2020.
29 S. Matsika, *Chemical Physics*, 2008, **349**, 356–362.
30 J. Segarra-Martí, T. Tran and M. J. Bearpark, *Physical Chemistry Chemical Physics*, 2019, **21**, 14322–14330.
31 M.-D. Su, in *Photochemistry and Photophysics*, eds. S. Saha and S. Mondal, IntechOpen, Rijeka, 2018, p. Ch. 6.
32 S. X. Tian, *Physical Chemistry Chemical Physics*, 2012, **14**, 6433–6443.
33 J.-P. Champeaux, P. Çarçabal, J. Rabier, P. Cafarelli, M. Sence and P. Moretto-Capelle, *Physical Chemistry Chemical Physics*, 2010, **12**, 5454–5461.
34 J. M. Rice, G. O. Dudek and M. Barber, *Journal of the American Chemical Society*, 1965, **87**, 4569–4576.
35 C. Zhou, S. Matsika, M. Kotur and T. C. Weinacht, *The Journal of Physical Chemistry A*, 2012, **116**, 9217–9227.
36 J. K. Wolken, C. Yao, F. Tureček, M. J. Polce and C. Wesdemiotis, *International Journal of Mass Spectrometry*, 2007, **267**, 30–42.
37 A. L. Padellec, P. Moretto-Capelle, M. Richard-Viard, J. P. Champeaux and P. Cafarelli, *Journal of Physics: Conference Series*, 2007,101 , 012007
38 M. Ryszka, R. Pandey, C. Rizk, J. Tabet, B. Barc, M. Dampc, N. J. Mason and S. Eden, *International Journal of Mass Spectrometry*, 2016, **396**, 48–54.
39 G. Sampoll, R. L. Watson, O. Heber, V. Horvat, K. Wohrer and M. Chabot, *Physical Review A*, 1992, **45**, 2903–2914.
40 M. C. Bacchus-Montabonel, *Chemical Physics Letters*,2016 ,**664,** 173-177